The chemistry of planet-forming disks: a story from inner to outer disk

Temmink, M.

Citation

Temmink, M. (2026, June 5). *The chemistry of planet-forming disks: a story from inner to outer disk*. Retrieved from https://hdl.handle.net/1887/4304669

PART II

Substructures in the outer disk

Chapter 5

MINDS: The influence of outer dust disk structure on the volatile delivery to the inner disk

Shortened version focused on the ALMA analysis of

D. Gasman, M. Temmink, E. F. van Dishoeck, N. T. Kurtovic, S. L. Grant, A. D. Sellek, B. Tabone, T. Henning, I. Kamp, M. Güdel, D. Barrado, A. Caratti o Garatti, A. M. Glauser, L. B. F. M. Waters, A. M. Arabhavi, H. Jang, J. Kanwar, J. L. Lienert, G. Perotti, K. Schwarz, M. Vlasblom

A&A, 694, A147 (2025)

Abstract

Context. Substructures, such as gaps and rings, have been proposed to play a unique role in setting the chemical reservoirs in the inner regions of planet-forming disks. In particular, radial drift has been proposed to enhance the inner disk (cold) H_2O reservoir. To investigate the influence of these substructures on the chemistry in the inner disk as seen with JWST-MIRI, detailed information on their location, width, and depth is required.

Aims. This work aims to find and characterise substructures at small radii (<20 au) in a sample of 8 disks that have existing high-resolution ALMA continuum, indicative of gaps and rings at larger radii, and JWST-MIRI/MRS observations.

Methods. The ALMA visibilities were fitted in the visibility plane. The modelled brightness profile was used to identify rings (local maxima) and gaps (local minima), and to determine the width and depth of the gaps. A curve-of-growth technique was used to constrain the dust disk size.

Results. Substructures were identified in all 8 disks, matching in many cases with the results of previous works at larger radii and finding new ones at smaller radii. Crucially, we have identified a small inner cavity (a width of ~9 au) in the disk of BP Tau and a deep inner gap in the disk of Sz 98 (at $R_{\rm gap}$ ~8.6 au). Upon visual inspection of the inferred radial profiles, additional plateaus were identified in the inner regions of the DR Tau, GW Lup, and IQ Tau disks, suggesting that even more substructures may be revealed with higher-resolution observations.

Conclusions. Since rings and gaps or plateaus are found within the inner 20 au of all modelled sources, substructures at radial distances of $\lesssim$15 au may be a common occurrence in disks. The role of the identified structures in setting the inner disk chemistry is, however, unclear. The strongest (cold) H_2O reservoir is seen for Sz 98, a disk with a deep gap located close to the host star, suggesting that the leakiness of the gaps is a crucial factor in setting the composition of the inner regions of planet-forming disks.

5.1 Introduction

This Chapter is part of the work by Gasman et al. (2025), which aimed to observationally assess the role of substructures in setting the inner disk's molecular reservoirs. In particular, the strength of the H_2O reservoir is thought to depend on the radial drift of icy pebbles. Banzatti et al. (2020) proposed a scenario in which small disks (R_{dust} ≤60 au) show an enhanced (cold, T ≤400 K) H_2O reservoir near its snowline due to efficient drift. Large and structured disks (R_{dust} ≥60 au) should, on the other hand, not show such an enhancement, as the drifting icy pebbles should be captured in the pressure traps. To test this scenario and to determine the role of pressure traps setting the inner disk composition, precise information on the location, width, and depth of the gaps - in particular, that of the gap closest to the host star - needs to be inferred from ALMA observations. Therefore, we employed visibility fitting techniques to obtain superresolution information on substructures that otherwise cannot be obtained from the resolution-limited images.

5.2 ALMA observations

In 2024, a sample of 8 disks was selected from all disks with existing JWST-MIRI/MRS observations, stellar masses of $M_{\odot}$ ≥0.45 $M_{\odot}$, and previously confirmed gaps in the millimetre dust continuum (see Gasman et al. 2025 for full details on the sample selection). Binary systems, sources with spiral features in the millimetre continuum emission, and highly inclined disks (i ≥70°) were excluded. The majority of the selected disks are part of the JWST Miri mid-INfrared Disk Survey (MINDS; Kamp et al. 2023; Henning et al. 2024) collaboration.

To study the presence of rings and gaps at small radii, we have retrieved the highest available spatial resolution ALMA observations publicly available for our sources. We list the distances, inclinations, position angles, and some of the observational properties in Table 5.1. Since for many of the sources, except BP Tau, the inclination and the position angle are well constrained, so we use the literature values while fitting the visibilities. For BP Tau, we estimated updated values using the CASA-task IMFIT by fitting an elliptical Gaussian. Additionally, we used IMFIT to estimate the phase offsets ($\Delta\alpha$ and $\Delta\delta$, both in arcsec) for each source and corrected for these offsets using the CASA-task FIXVIS. For some sources (CI Tau and GW Lup), additional shifts were determined from the image plane, ensuring that the peak flux in the model falls on the same position as the peak flux in the image. For only three of our sources (CI Tau, DR Tau, and IQ Tau), self-calibration yielded an increased signal-to-noise ratios (S/N). Therefore, we performed two rounds of phase-only self-calibration (solution intervals of 'inf' and '30s') for these sources. We have imaged (down to a threshold of 1.5× the root-mean square) the dust continuum of all our sources using the 'Briggs' weighting scheme with a robust parameter of +0.5. Figure 5.1 displays the continuum images and the resolving beams are highlighted in Table 5.1.

Table 5.1: Source properties and band 6 ALMA observations of the eight T Tauri disks.

Source	Inc. [°]	PA [°]	ALMA PID (PI)	Frequency [GHz]	Reference frequency [GHz]	Reference wavelength [mm]	Beam ["×" (°)]	Ref.
BP Tau	23.6	163.9	2019.1.00607.S (F. Long)	215-234	230.7	1.3	0.034×0.020 (-2.5)	This work
CI Tau	50.0	11.2	2016.1.01370.S (C. Clarke)	223-243	224.0	1.3	0.046×0.032 (15.9)	Long et al. (2018)
DL Tau	45.0	52.1	2016.1.01164.S (G. Herczeg)	217-234	218.0	1.4	0.133×0.108 (-2.3)	Long et al. (2018)
DR Tau	5.4	3.4	2016.1.01164.S (G. Herczeg)	217-234	218.0	1.4	0.128×0.100 (38.3)	Long et al. (2019)
GW Lup	38.7	37.7	2016.1.00484.L (S. Andrews)	230-248	232.6	1.3	0.030×0.023 (-89.2)	Huang et al. (2018a)
IQ Tau	62.1	42.4	2016.1.01164.S (G. Herczeg)	217-234	218.0	1.4	0.157×0.106 (-28.0)	Long et al. (2018)
Sz 98	47.1	111.6	2018.1.01458.S (Yen, H-W)	217-234	233.0	1.3	0.056×0.043 (27.3)	Tazzari et al. (2017)
V1094 Sco	53.0	109.0	2017.1.01167.S (S. Perez)	229-248	232.5	1.3	0.054×0.043 (-73.9)	van Terwisga et al. (2018)

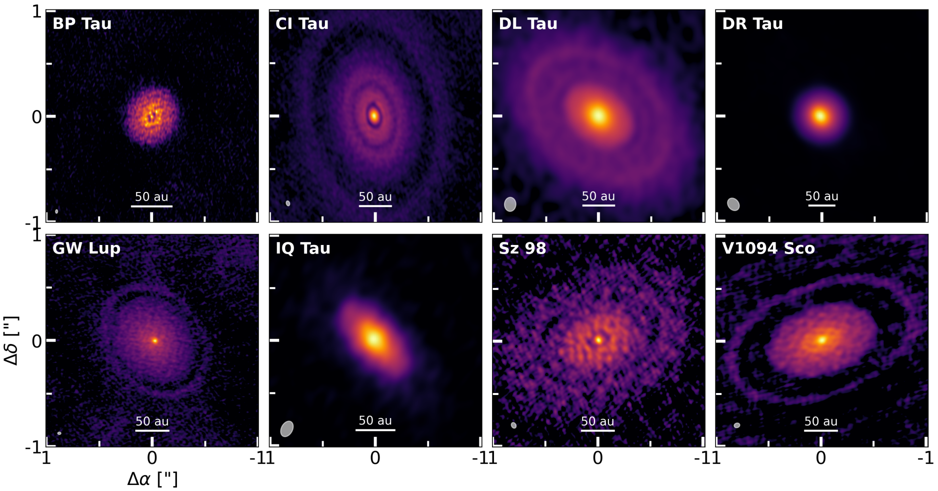

Figure 5.1: ALMA continuum images of the various sources. The images of CI Tau, DL Tau, GW Lup, Sz 98, and V1094 Sco have been imaged with a square-root scaling to reveal the weaker rings in the outer regions. The resolving beams are displayed in the lower left corner and the horizontal bars indicate scales of 50 au.

5.3 Visibility fitting

Given the non-uniformity of the ALMA sample, we have fitted the visibilities to infer potentially 'hidden' substructures in the disks that cannot be retrieved from the cleaned images. We have followed the approach by Zhang et al. (2016), where a Hankel transform acts as the link between the deprojected uv-distance and the radial brightness distribution ($I(\theta)$; Pearson 1999:

$$u' = (u\cos(\phi) - v\sin(\phi)) \times \cos(i), \tag{5.1}$$

$$v' = u\sin(\phi) + v\cos(\phi), \tag{5.2}$$

$$V(\rho) = 2\pi \int_0^\infty I_\nu(\theta)\theta J_0(2\pi\theta\rho)\mathrm{d}\theta. \tag{5.3}$$

Here, i and ϕ are the disk's inclination and position, $\rho = \sqrt{u'^2 + v'^2}$ denotes the deprojected uv-distance (given in units of λ, and θ is the radial angular scale as seen from the disk's centre. Finally, J_0 denotes the zeroth-order Bessel function of the first kinds. The model brightness distribution consists of a set of Gaussian functions, inspired by the peaks seen in the visibilities and modulated by a sinusoidal function that has a spatial frequency of ρ_i,

$$\begin{aligned} I(\theta) = & \frac{a_0}{\sqrt{2\pi}\sigma_0} \exp\left(\frac{\theta^2}{-2\sigma_0^2}\right) + \\ & \sum_i \cos\left(2\pi\theta\rho_i\right) \times \frac{a_i}{\sqrt{2\pi}\sigma_i} \exp\left(-\frac{\theta^2}{2\sigma_i^2}\right). \end{aligned} \tag{5.4}$$

This function yields the $\{a_0,\, \sigma_0,\, a_i,\, \sigma_i,\, \rho_i\}$ as the set of free parameters. For our sample, we report the minimum of additional Gaussian functions that results in a good fit to all the visible features in the visibilities.

We have deprojected the visibilities using the inclinations and position angles listed in Table 5.1. To ensure that we are able to fit the visibilities properly, we have visually compared the visibilities of all spectral windows (line and continuum) with those of the continuum spectral windows alone. For the line spectral windows, we masked visible lines, ensuring that they only contain continuum emission. In the cases of DR Tau, GW Lup, and Sz 98, we found that the uncertainties of the visibilities of the continuum spectral windows were significantly lower than those when including all spectral windows. Therefore, we only used the continuum spectral windows for those three sources. In addition, we only use the continuum spectral windows for DL Tau, as the measurement set was obtained through private communication. For the four other sources we have used all spectral windows.

We bin the visibilities to speed up the fitting process, using the implementation of the FRANKENSTEIN-code (Jennings et al. 2020), and we avoid fitting the visibilities with large scatter, generally occurring at larger values of kλ. For BP Tau, DL Tau, DR Tau, Sz 98, and V1094 Sco we limit the visibilities to $\leq$2000 kλ, whereas we limit the visibilities of CI Tau and GW Lup to $\leq$3000 kλ. Finally, the visibilities of IQ Tau are limited to $\leq$1500 kλ. In addition, the visibilities are binned to widths of 1-2$\times 10^4$ λ. We fit the visibilities using the Markov Chain Monte Carlo (MCMC) implementation of the EMCEE-package (Foreman-Mackey et al. 2013). The fitting was performed two-fold, similarly to the approach carried out by Long et al. (2018): in the first round, we used 2500 iterations to explore the prior space, identifying the best-fit parameters. In the second round, we used 10,000 iterations to explore a confined parameter space around these best-fit parameters. From this second round, we use a final 5000 iterations to identify the median values of the posterior distributions. The lower and upper uncertainties are, respectively, taken to be the 16th and 84th percentiles. Our fitting results are listed in Table 5.2 and the fits to the visibilities are presented in Figure 5.2.

Table 5.2: Median values from the fitting posterior distributions and the corresponding uncertainties.

Source	a_i [a.u.]	σ_i ["]	ρ_i [kλ]
BP Tau	104^{+5}_{-10}	$0.17^{+0.04}_{-0.02}$	-
	17^{+39}_{-14}	$0.28^{+0.07}_{-0.04}$	251^{+35}_{-37}
	2 ± 6	0.48 ± 0.07	818^{+58}_{-66}
	13^{+7}_{-6}	$0.21^{+0.06}_{-0.05}$	904^{+62}_{-38}
	-17^{+6}_{-7}	0.07 ± 0.03	719^{+62}_{-67}
CI Tau	186^{+20}_{-15}	0.46 ± 0.02	-
	135^{+35}_{-26}	0.43 ± 0.04	161^{+8}_{-9}
	45^{+21}_{-14}	0.45 ± 0.06	388 ± 14
	120^{+24}_{-29}	$0.08^{+0.03}_{-0.01}$	516^{+66}_{-61}
	28^{+22}_{-16}	$0.29^{+0.07}_{-0.05}$	544^{+42}_{-43}
	111^{+23}_{-26}	0.17 ± 0.03	1018^{+26}_{-25}
	63^{+16}_{-29}	$0.16^{+0.07}_{-0.04}$	1401^{+63}_{-43}
	27^{+18}_{-15}	$0.22^{+0.05}_{-0.04}$	1714^{+53}_{-55}
DL Tau	251 ± 10	0.39 ± 0.01	-
	208^{+28}_{-20}	0.33 ± 0.01	215 ± 3
	172 ± 4	$0.11^{+0.02}_{-0.01}$	527^{+11}_{-13}
	48^{+19}_{-11}	$0.39^{+0.06}_{-0.05}$	853 ± 6
	92 ± 9	0.30 ± 0.03	1194^{+10}_{-12}
	77^{+7}_{-9}	$0.49^{+0.03}_{-0.02}$	1371 ± 4
	99 ± 5	0.22 ± 0.01	1731^{+7}_{-5}
DR Tau	461^{+17}_{-21}	0.16 ± 0.01	-
	179^{+60}_{-65}	$0.21^{+0.02}_{-0.01}$	329^{+21}_{-20}
	210 ± 8	0.09 ± 0.01	807^{+28}_{-30}
	99 ± 7	$0.16^{+0.01}_{-0.02}$	1692 ± 16
GW Lup	100^{+30}_{-22}	0.31 ± 0.02	-
	106^{+11}_{-14}	$0.18^{+0.04}_{-0.05}$	208^{+36}_{-56}
	62^{+8}_{-9}	$0.14^{+0.04}_{-0.03}$	688^{+49}_{-58}
	26 ± 8	$0.36^{+0.06}_{-0.05}$	1113 ± 22
	25 ± 6	0.17 ± 0.04	1414^{+47}_{-49}
	12 ± 5	$0.42^{+0.07}_{-0.06}$	1819^{+31}_{-32}
IQ Tau	69^{+28}_{-20}	0.36 ± 0.03	-
	64^{+15}_{-18}	$0.26^{+0.06}_{-0.03}$	135^{+54}_{-31}
	23 ± 4	0.34 ± 0.06	528^{+17}_{-16}
	11^{+5}_{-4}	$0.33^{+0.07}_{-0.06}$	1013^{+38}_{-45}
	10 ± 4	0.92 ± 0.07	1200^{+13}_{-16}
Sz 98	143^{+7}_{-4}	0.40 ± 0.01	-
	81^{+9}_{-8}	$0.42^{+0.02}_{-0.03}$	216^{+3}_{-4}
	31^{+17}_{-7}	$0.16^{+0.04}_{-0.03}$	661^{+30}_{-29}
	16 ± 4	$0.55^{+0.07}_{-0.05}$	994^{+12}_{-13}
	29^{+4}_{-3}	$0.45^{+0.05}_{-0.04}$	1258^{+9}_{-8}
	104^{+12}_{-15}	0.04 ± 0.01	1449^{+65}_{-54}
V1094 Sco	131^{+11}_{-16}	$0.66^{+0.04}_{-0.03}$	-
	166 ± 6	$0.48^{+0.04}_{-0.05}$	124 ± 5
	61^{+8}_{-7}	$0.68^{+0.04}_{-0.05}$	261 ± 4
	57^{+6}_{-11}	0.38 ± 0.03	430 ± 5
	33 ± 4	0.19 ± 0.07	709^{+31}_{-35}
	31 ± 8	0.46 ± 0.05	943^{+9}_{-8}
	41^{+4}_{-5}	$0.51^{+0.05}_{-0.06}$	1173 ± 7
	29 ± 4	0.41 ± 0.06	1368 ± 12
	16 ± 3	0.36 ± 0.06	1619^{+17}_{-18}

Notes. Gaussian function fit parameters a_i, σ_i, and ρ_i, describing the intensity, width, and spatial frequency, respectively (see Eq. 5.4).

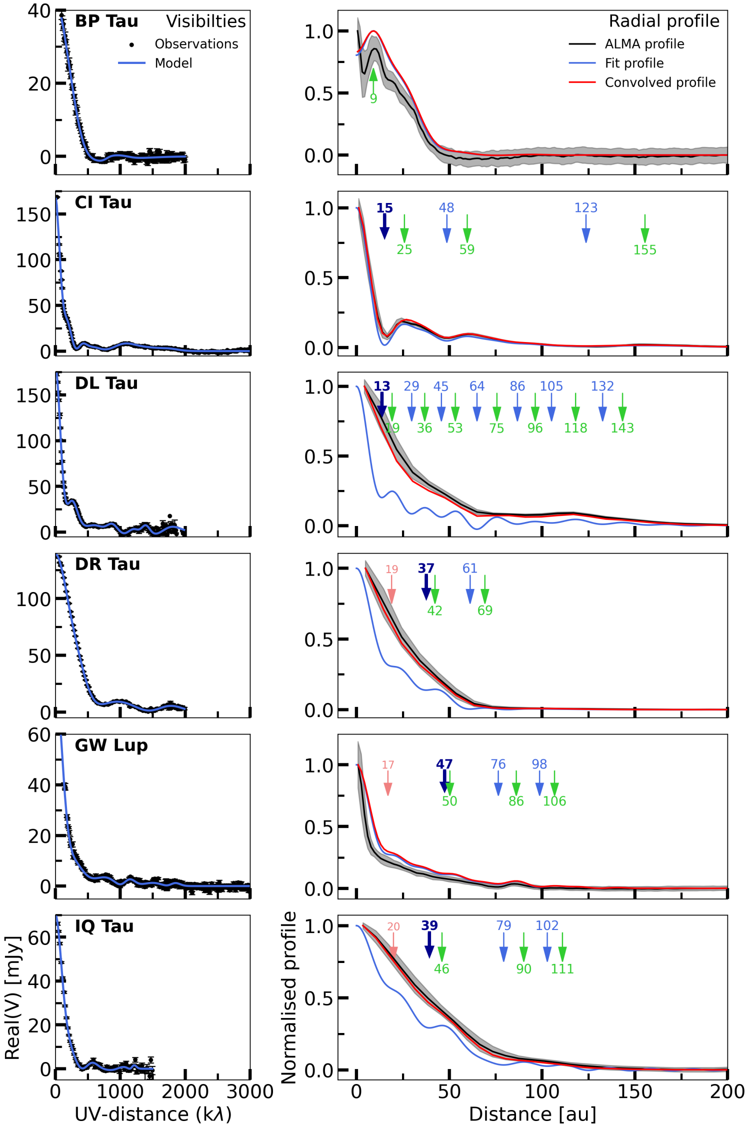

Figure 5.2: Fit to the visibilities (blue line in the left panels for each source) and the various radial profiles (right panels): one from the ALMA image (black line), the model radial profile (blue line), and the radial profile from the model convolved with a Gaussian kernel tailored after the resolving beam (red line). The gaps and rings (or local minima and maxima) and plateaus/shoulders are indicated by, respectively, the blue, green, and red arrows, where the values indicate their integer radial positions. The location of the innermost gap is emphasised by the dark blue arrows. The shaded grey area indicates the standard deviation in each radial bin of the ALMA profile.

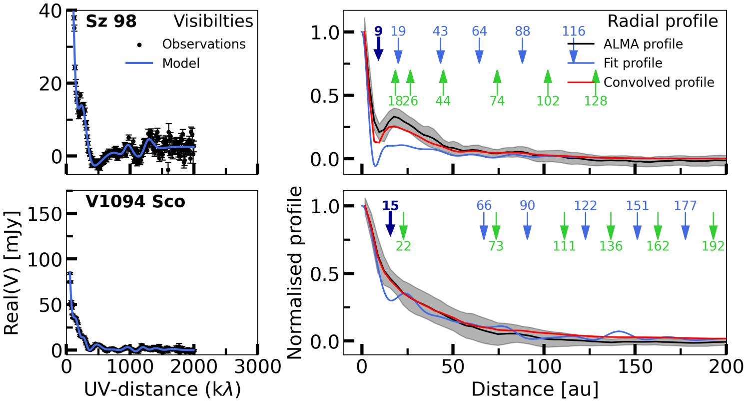

Figure 5.2: Continuation of Figure 5.2.

5.4 Characterising the millimetre continuum emission

Using the radial brightness distribution from median values of the posterior distributions, we infer the radial locations of substructures. The locations of rings ($r_{\rm r}$) and gaps ($r_{\rm g}$) are identified through, respectively, the local maxima and minima present in the radial profiles. Other structures, such as 'shoulders' or 'plateaus', visible in the radial profiles are visually identified. To characterise the depth and widths of the identified gaps, we follow the approach of Huang et al. (2018a). Here, the gap depth is defined as the ratio of the gap intensity ($I_{\rm g}$) and that of the neighbouring ring with the smallest flux contrast ($I_{\rm r}$), $\Delta I_{\rm g} = I_{\rm g}/I_{\rm r}$. Given the ratio, the gaps with the smallest value reported for the depth are the deepest ones. The width of the gap is determined as the radial width between the inner and outer edges of the gaps ($r_{\rm g,i}$ and $r_{\rm g,o}$), which are the radial locations where the intensity equals $I_{\rm mean} = 0.5\,(I_{\rm g} + I_{\rm r})$. Therefore, the width is given by $\Delta r_{\rm g} = r_{\rm g,o} - r_{\rm g,i}$.

We also determine the continuum disk radius ($R_{\rm disk}$) using a curve-of-growth method (see also Ansdell et al. 2016 and/or Stapper et al. 2022 for more information) for radii containing 68%, 90%, and 95% of the flux density. The values for the disk radii are listed in Table 5.3. In short, we use aperture photometry to investigate at what radius the flux density within the apertures flattens off. We increase the apertures by the pixel size and limit our range to where we see no significant substructures in the ALMA radial profiles, as we are only using high-resolution observations, and therefore we may lack the resolving power for weak outer disk features.

The model radial profiles, together with the identified gaps and rings, are presented in Figure 5.2. In particular, we have highlighted the gap that is located closest to the host star. Here, we also show the ALMA continuum image and the model radial profile convolved with a Gaussian kernel tailored after the ALMA resolving beam. The convolved radial profiles clearly show that the beam is respon-

Table 5.3: Identified substructures and dust continuum sizes for the sources.

Source	r_g	r_r	Δr_g	ΔI_g	R_disk (Model/ALMA)$^{(a)}$		
	[au]	[au]	[au]		68% [au]	90% [au]	95% [au]
BP Tau	-	9	-	-	30.0/29.0	40.6/38.1	46.7/44.7
CI Tau	**15.2**	25.9	7.8	0.10	105.3/114.2	172.5/180.3	189.3/199.4
	48.7	59.7	9.4	0.59			
	123.7	155.5	27.2	0.59			
DL Tau	**13.8**	19.2	4.5	0.81	112.0/115.2	147.2/156.8	163.2/176.0
	29.9	37.0	5.9	0.65			
	45.9	53.3	7.0	0.59			
	65.0	75.9	9.6	-0.44			
	86.7	96.2	7.7	0.38			
	105.0	117.9	8.2	0.66			
	132.6	143.2	9.3	0.46			
DR Tau	**37.7**	42.3	3.9	0.96	39.0/42.9	54.6/66.3	89.7/97.5
	61.2	*69.2*	6.0	0.33			
GW Lup	***47.5***	*50.4*	2.4	0.99	67.4/65.1	102.3/110.8	115.5/134.1
	76.5	86.1	11.0	0.56			
	98.7	106.8	6.5	0.54			
IQ Tau	**39.3**	46.1	5.7	0.95	58.0/68.6	103.0/118.8	118.8/145.2
	79.3	*90.2*	10.2	0.62			
	102.8	*111.0*	7.5	0.73			
Sz 98	***8.6***	*16.4*	4.6	-0.72	109.8/107.3	147.3/146.0	159.7/162.2
	19.3	*27.3*	3.1	0.97			
	42.8	*45.3*	2.1	1.00			
	64.3	*74.3*	8.9	0.63			
	88.1	*102.0*	13.3	0.21			
	116.0	*128.0*	10.5	0.61			
V1094 Sco	***15.6***	*22.8*	5.8	0.85	162.4/131.4	239.3/238.1	255.4/256.7
	67.0	*73.7*	6.4	0.92			
	90.8	111.2	14.3	0.40			
	122.8	*136.7*	9.8	0.22			
	151.2	*162.5*	9.5	0.37			
	177.6	193.0	12.0	0.37			
	200.2	*217.2*	6.8	0.95			

Notes. $^{(a)}$We list the values for the outer dust disk radii retrieved from both the model image and from the ALMA image. The value before the slash is obtained from the model images, whereas the value after the slash is obtained from the ALMA image. r_g, r_r, Δr_g, and ΔI_g are the gap location, ring location, gap width and depth, respectively. The values used as R_gap in the analysis of the JWST/MIRI-MRS data are highlighted in boldface. The values listed in italics are newly identified substructures in this work.

sible for smoothing out weak structures in the ALMA images and, subsequently, that these features cannot be distinguished from analysis in the image plane. All the retrieved locations of the gaps and the rings, and the gap widths and depths are listed in Table 5.3. Additionally, in Figure 5.3 we display a comparison between the ALMA continuum image, the model image, the model image convolved with a Gaussian kernel, and the residuals. The residuals are obtained by subtracting the convolved model image off the ALMA image. Similarly to what is seen for the radial profiles, the convolution with the Gaussian kernel smooths out the various weak substructures visible in the model and therefore become unidentifiable in the images.

Besides the various gaps and rings, we also visually identified a few plateaus, which may hint at additional substructures. These plateaus are indicated by the red arrows in Figure 5.2. To summarise, we identify three plateaus: in DR Tau at ~19 au, in GW Lup at ~17 au, and in IQ Tau at ~20 au.

Overall we find that the convolved images represent the ALMA images quite well, but there are some residuals that require attention. The residuals of BP Tau are mostly negative, indicating larger flux in the model image following the identified cavity in the models. The central, unresolved spot in the ALMA image may be attributed to free-free emission or emission from the host star itself (see e.g. Rota et al. 2024). For CI Tau, the residuals show that clear asymmetric structures are found in the ALMA image. These residuals show that the outer edges of the gap are not perfectly oval shaped as they are in the model. DL Tau, DR Tau, and IQ Tau all three show clear residuals in the central positions. These asymmetries likely arise from sub-pixel offsets between the peaks of the ALMA images and the model images. We note that the observations for these sources have the lowest spatial resolution (~0.11"), which provides a potential explanation why these residuals are the largest. Higher resolution observations will likely provide better fits and cleaner residuals. The residuals of GW Lup are dominated by the model overfitting the width of the inner region, as can also be seen from the radial profiles (see Figure 5.2). Additionally, there may be a sub-pixel offset for the location of the maximum flux in the ALMA image, which causes the asymmetric feature to appear in the residuals. For both Sz 98 and V1094 Sco, we see that the residuals are rather patchy, which may be caused by the use of only the highest resolution observations available. Combining these observations with those of lower resolution, which are better at resolving the largest scales, may improve the residuals.

5.5 Comparison with previous works

Nearly all disks, except Sz 98, have been modelled before, so we compare the inferred substructures:

BP Tau: BP Tau has previously been fitted by Zhang et al. (2023), but no fits have been carried out for the high-resolution observations used in this work. We note that the models of Zhang et al. (2023) already point towards a small cavity in this disk, which now seems confirmed by our results.

CI Tau: The high-resolution CI Tau observations used in this work have previously been modelled by Clarke et al. (2018) and Rosotti et al. (2021). They find radial locations for the gaps of ~12, ~45, and ~114 au, and radii of ~23, ~54, and ~114 au for the rings. Generally, these values are close to our values, except

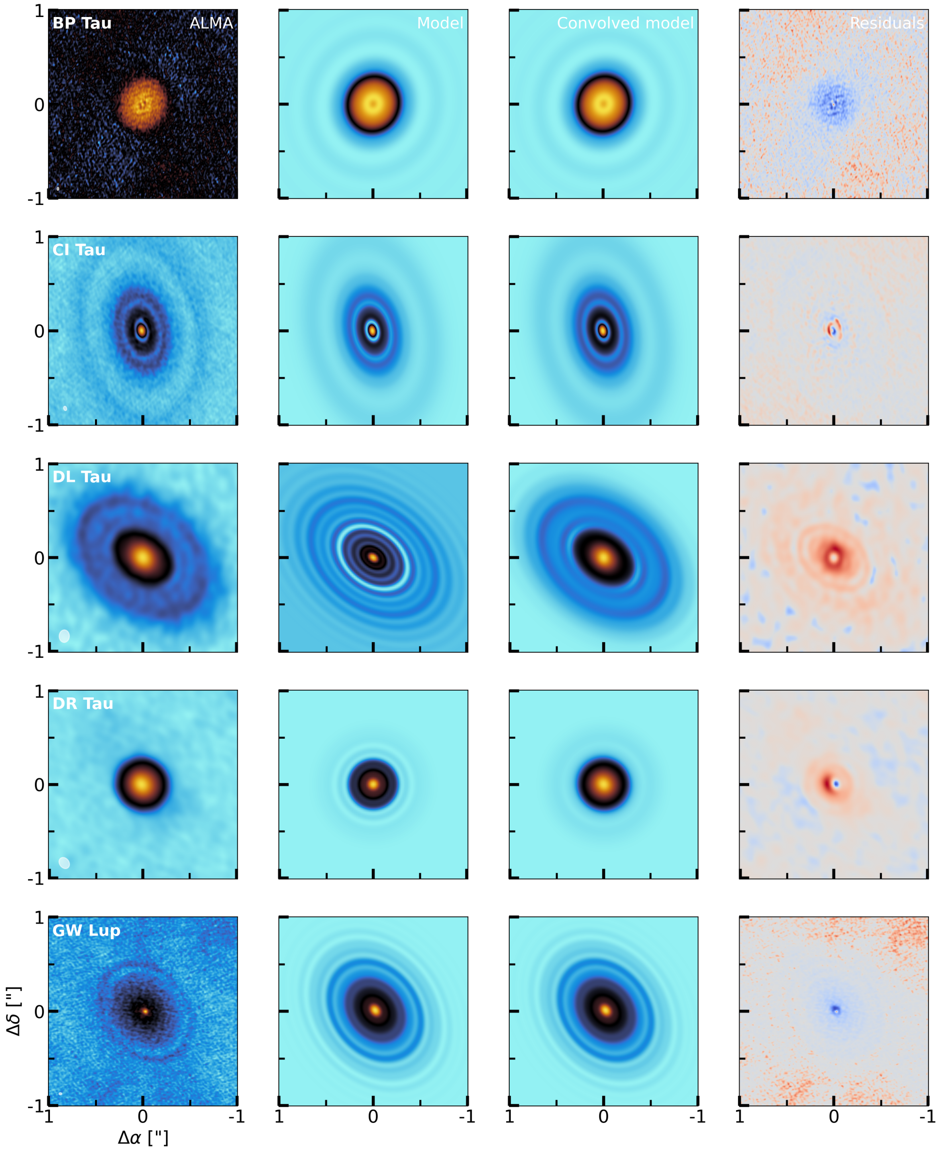

Figure 5.3: Comparison between the ALMA image (first column), the model image (second column), the convolved model (third column), and the residuals (final column). All images, except the residuals, are shown with an arcsinh-stretch colourmap. The residuals are taken by subtracting the convolved model image off the ALMA image. Here, red residuals indicate more flux in the ALMA image, whereas blue residuals indicate more flux in the convolved model image.

for the outer most ring, for which we find a larger value of ∼155 au.

DL Tau: DL Tau has been modelled by Zhang et al. (2023) using the same tech-

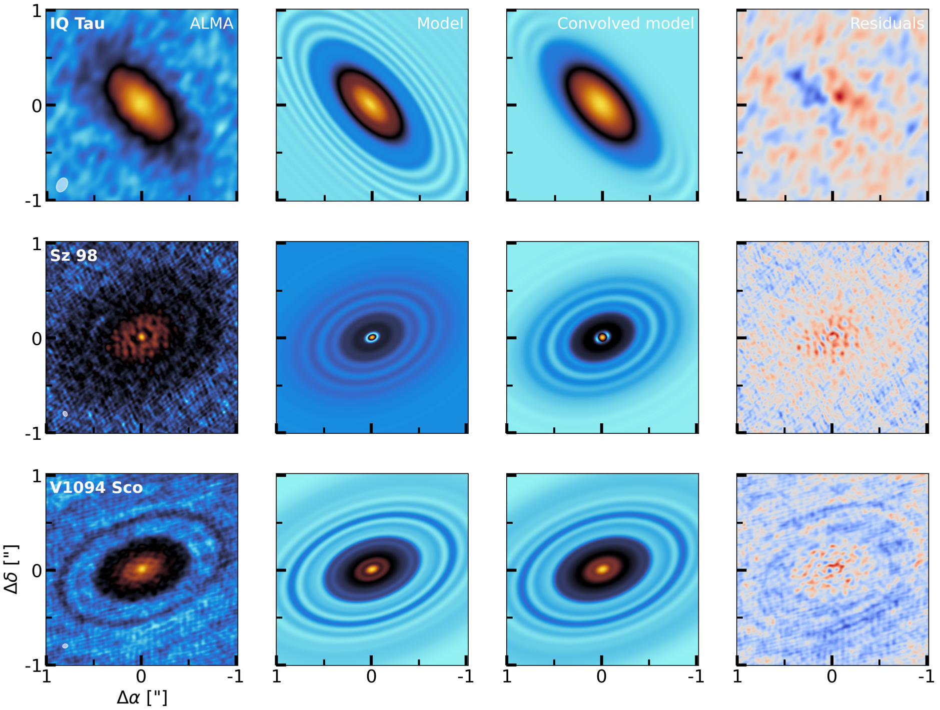

Figure 5.3: Continuation of Figure 5.3.

nique, but also has been given an extensive treatment by Jennings et al. (2022b). Both works yield similar radial brightness profiles. In addition, Zhang et al. (2023) lists gap locations of ∼15, ∼31, ∼47, ∼66, ∼95, and ∼129 au, which all fall within 10 au of our listed values. The fit by Zhang et al. (2023) suggests deeper gaps. As is seen in Figure 5.2 our convolved profile does not fully match the ALMA profile, suggesting that our modelled rings are not as strong as those of Zhang et al. (2023), yielding smaller gap depths.

DR Tau: Similar to DL Tau, DR Tau has been modelled by Jennings et al. (2022b) and Zhang et al. (2023). Again, our respective brightness profiles are rather similar, except we find an additional potential substructure gap-ring combination at, respectively, 61.2 and 69.2 au. The other gaps are found at similar locations, although the first gap identified by Zhang et al. (2023) (∼18 au) appears as a plateau in our profile.

GW Lup: GW Lup was modelled by Jennings et al. (2022a), who finds a similar looking brightness profile, with a plateau in the inner regions (<0.1"). Overall, we find a few more potential substructures in addition to the well-known ring at 86 au.

IQ Tau: IQ Tau has also been modelled by Zhang et al. (2023). We find the same location for the gap-ring combination around ∼40 au. However, the outer two rings identified in our work are not found in their work. Higher spatial resolution and sensitivity observations may proof the validity if these substructures do indeed exist or not.

V1094 Sco: These higher resolution observations of V1094 Sco have not been modelled before, but van Terwisga et al. (2018) modelled lower resolution (~0.18") data. They only provided locations for gaps located at 100 and 170 au. Our fit to the higher resolution observations thus provide hints for potentially more substructures, with the most notable gap at ~16 au.

5.6 Identified structures, snowlines, and proposed scenarios

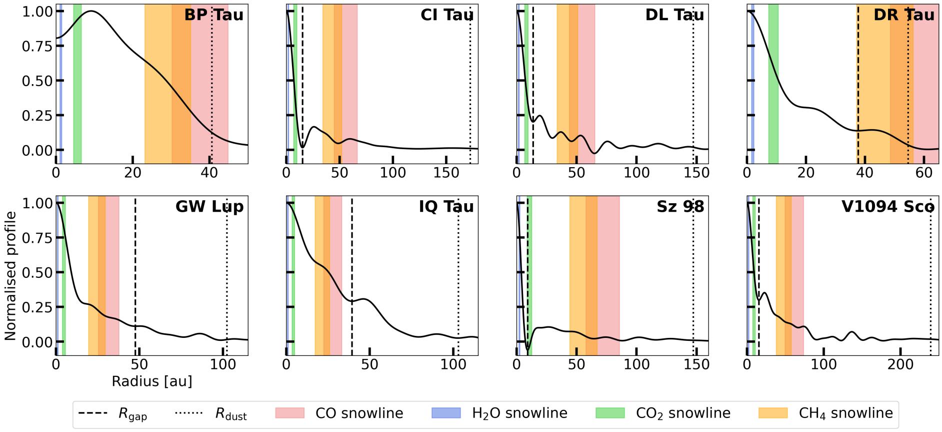

Figure 5.4: Normalised, modelled radial profiles of the ALMA observations. The blue, green, orange, and red shaded areas indicate estimated locations of, respectively, the H_2O, CO_2, CH_4, and CO snowlines (Gasman et al. 2025). The dashed line displays the position of the closet-in identified gap, while the dotted line indicates the 90% dust disk radius (see Table 5.3).

To investigate the role of the innermost gap, its location was compared with the estimated locations of the H_2O, CO_2, CH_4, and CO snowlines in Gasman et al. (2025) (see also Figure 5.4). For all disks, the H_2O snowline was found to be located inwards of the innermost gap. This also holds mostly for the CO_2 snowline, except for Sz 98, where the snowline is located towards the outer edge of the gap. Conversely, the CH_4 and CO appear to be mostly located beyond the first gap, except in the cases of GW Lup and IQ Tau.

Based on the locations of the gaps and the snowlines, the strengths of the different molecular reservoirs (H_2O, CO_2, HCN, and C_2H_2) seen in the JWST-MIRI/MRS spectra were compared with different scenarios put forward by existing models (Kalyaan et al. 2021, 2023; Mah et al. 2024; Lienert et al. 2024; Sellek et al. 2025). These scenarios explore the change of the inner disk composition from oxygen-rich (or H_2O-rich) to carbon-rich over the disk's lifetime, considering gaps at different locations and three levels of leakiness to drifting pebbles: leaky, moderately leaky, and not leaky. The transition from an oxygen-rich to carbon-rich is expected to occur naturally during the evolution of a disk, however, the age at which this happens is related to the location and leakiness of the innermost gap. Given the uncertainties in the ages, multiple scenarios were deemed likely for each disks. Therefore, the exact scenario and role of substructures in setting the inner disk composition could not be pinpointed.

Most notably, Sz 98 is a large disk ($R_{\rm dust}$ $\gg$100 au) with a deep gap located very close to the host star ($r_{\rm g}$ $\sim$8.6 au). Intuitively, this disk should have not have an enhanced cold H_2O reservoir following the scheme proposed by Banzatti et al. (2020). Yet, this disk has the strongest cold H_2O reservoir of the entire sample. Therefore, the small dust grains and the gas may not be impeded by the gap from radially moving inwards, and the leakiness of the gaps is very likely crucial in setting the inner disk reservoirs. More details and searches for correlations with the observed JWST-MIRI line fluxes are presented in Gasman et al. (2025).

5.7 Concluding remarks

Visibility fitting techniques are a powerful tool to identify and characterise substructures in planet-forming disks. Gaps and rings are found in all 8 analysed disks, including the confirmation of a small cavity in the disk of BP Tau and a deep gap at $\sim$8.6 au in the disk of Sz 98. Many of the found substructures match those proposed in other works, yet additional gaps are proposed in the disks of GW Lup, IQ Tau, and V1094 Sco. Furthermore, visual inspection leads to the identification of plateaus - potentially further substructures - in the inner regions ($\sim$17-20 au) of the disks of DR Tau, GW Lup, and IQ Tau. As all disks show substructures or plateaus within the inner 20 au, we propose that substructures at radial distances of $\lesssim$15 au may be a common occurrence in planet-forming disks.

Given large uncertainties in the ages of the systems, the role of substructures in setting the inner disk composition with time could not be established. The case of Sz 98 is of particular interest, as this large and structured disk shows particularly strong emission from the cold H_2O reservoir. A deep gap was identified close to the host star, yet it may be leaky to small dust grains and the gas, still replenishing the inner regions with fresh material. Therefore, it is thought that the leakiness of the gaps plays a crucial role in setting the inner disk composition of planet-forming disks.